

# Sensors & Diagnostics

Volume 2  
Number 1  
January 2023  
Pages 1–246

[rsc.li/sensors](https://rsc.li/sensors)



ISSN 2635-0998







## PAPER

Andrew J. de Mello, Daniel A. Richards *et al.*  
Real-time, smartphone-based processing of lateral flow assays  
for early failure detection and rapid testing workflows



Cite this: *Sens. Diagn.*, 2023, 2, 100

# Real-time, smartphone-based processing of lateral flow assays for early failure detection and rapid testing workflows†

Monika Colombo,  ‡ Léonard Bezingue,  ‡ Andres Rocha Tapia,   
 Chih-Jen Shih,  Andrew J. de Mello  \* and Daniel A. Richards  \*

Despite their simplicity, lateral flow immunoassays (LFIsAs) remain a crucial weapon in the diagnostic arsenal, particularly at the point-of-need. However, methods for analysing LFIsAs still rely heavily on sub-optimal human readout and rudimentary end-point analysis. This negatively impacts both testing accuracy and testing times, ultimately lowering diagnostic throughput. Herein, we present an automated computational imaging method for processing and analysing multiple LFIsAs in real-time and in parallel. This method relies on the automated detection of signal intensity at the test line, control line, and background, and employs statistical comparison of these values to predictively categorise tests as “positive”, “negative”, or “failed”. We show that such a computational methodology can be transferred to a smartphone and detail how real-time analysis of LFIsAs can be leveraged to decrease the time-to-result and increase testing throughput. We compare our method to naked-eye readout and demonstrate a shorter time-to-result across a range of target antigen concentrations and fewer false negatives compared to human subjects at low antigen concentrations.

Received 3rd November 2022,  
 Accepted 30th November 2022

DOI: 10.1039/d2sd00197g

[rsc.li/sensors](https://rsc.li/sensors)

## 1. Introduction

Since their introduction in the late 1980s,<sup>1</sup> paper-based lateral flow immunoassays (LFIsAs) have become indispensable tools for rapid, low-cost diagnostic testing.<sup>2</sup> LFIsAs are routinely used to detect a plethora of conditions,<sup>3</sup> though their greatest medical utility arguably lies in infectious disease diagnosis. Indeed, due in large part to the COVID-19 pandemic, LFIsAs are now synonymous with rapid, point-of-need testing.<sup>4,5</sup> The ability to rapidly and affordably test large populations is invaluable during infectious disease outbreaks and crucial to successful track-trace-treat pathways.<sup>6</sup> Moreover, mass testing can be leveraged to develop epidemiological models,<sup>7</sup> monitor vaccine efficacy,<sup>8</sup> and ultimately improve our understanding of diseases. Effective mass testing is contingent upon rapid diagnostic tests that can be reliably delivered, used, and analysed in populations most affected by the target disease, *i.e.* where demand is highest. As exemplified by the ongoing COVID-19 pandemic, LFIsAs are key to meeting this demand.

By circumventing the need for centralised facilities and highly-trained personnel, LFIsAs can significantly increase testing throughput. However, due to multiple limitations, these gains are yet to be fully realised.<sup>9</sup> Naked-eye readout, whilst advantageous for accessibility and affordability, relies on human interpretation. This can lead to both false positives and false negatives as a result of misunderstandings and conscious bias.<sup>10</sup> Misunderstandings can result from an impaired ability to correctly distinguish and observe test/control lines or an inability to detect device failure.<sup>11</sup> Conscious bias can be introduced when certain test outcomes are more desirable and incentives for dishonesty exist, such as the ability to attend social events or travel freely.<sup>12</sup> Improvements in telemedicine have been developed in response to these issues, although they are far from perfect.<sup>13</sup> Thus, despite the fact that LFIsAs are compatible with self-testing, the practical reality is that these assays are still predominantly performed in mass testing centres or local medical facilities. A lack of parallelisation and connectivity also limits the throughput of LFIA testing; tests are typically performed one at a time by a single user, manually interpreted, and then the results are logged on a separate system. Such a workflow slows down the testing process and introduces multiple opportunities for human error. Integrating LFIsAs into highly automated and parallelised workflows, in which multiple tests can be run, analysed, and reported with minimal human intervention and interpretation, is key to overcoming these limitations.

*Institute for Chemical and Bioengineering, ETH Zurich, Vladimir-Prelog-Weg 1, 8093 Zürich, Switzerland. E-mail: andrew.demello@chem.ethz.ch, daniel.richards@chem.ethz.ch*

† Electronic supplementary information (ESI) available. See DOI: <https://doi.org/10.1039/d2sd00197g>

‡ Both authors contributed equally.



Realising this, researchers have started to develop computerised lateral flow readers. These readers come in the form of both highly integrated stand-alone devices<sup>14–17</sup> and software Apps that rely on existing hardware within smartphones and tablets.<sup>18–20</sup> These developments demonstrate that replacing human interpretation with automated computational analysis yields benefits in terms of accuracy and reproducibility, ultimately improving test reliability.<sup>21</sup> However, the vast majority of these devices still read only one test at a time. Though some parallelised approaches exist,<sup>22</sup> they rely on end-point readings and cannot detect common assay failures caused by human error or device malfunction. Clearly, there is a need for innovation in this space if LFIAs are to reach their full potential.

Herein we report a novel computational image analysis algorithm capable of processing, analysing, and interpreting multiple LFIA tests in parallel. Inspired by the work of Miller *et al.*,<sup>23</sup> who employed continuous imaging to derive binding kinetics in lateral flow systems, our method uses computational image analysis to simultaneously examine the flow profile, test (T) line, and control (C) line of lateral flow assays as they are running. We demonstrate that by continuously monitoring the intensity change at the test line, the algorithm can accurately predict end-point colour density and determine assay results for multiple LFIAs in real-time. Furthermore, we show that by analysing the flow profile and control line we can detect several common early failure scenarios and ultimately determine the validity of LFIAs as they are running. The method is supported by a simple 3D-printed housing, and the custom code can be run entirely on a smartphone (Fig. 1). Using a commercial LFIA

for SARS-CoV-2 nucleocapsid, we demonstrate that this approach leads to significant improvements over standard human interpretation, in terms of both time-to-result and testing throughput.

## 2. Results and discussion

The LFIA processing platform consists of a modular 3D-printed housing that can accommodate up to eight strips (Fig. 1 and S1†). Each strip is held by an individual insert (Fig. S2†), with the inserts being independently interchangeable (random access). Once inserted, the strips are imaged using a smartphone mounted atop the enclosure. The setup ensures consistent positioning of the strips and uniform lighting conditions using the integrated smartphone flashlight. The smartphone runs a bespoke App that identifies and analyses the strips in parallel. The App leverages computational methods and statistical analytics to 1) quantify and interpret the test results and 2) detect and identify technical failures at an early stage. All these processes are performed in parallel and in real time.

### 2.1 Statistical line detection

Traditional LFIA readout relies on qualitative/semi-quantitative assessment of the colour intensity at the test line (test line intensity) once the test has reached completion (the end point). This end-point intensity is highly influenced by the initial binding kinetics between the disease target (labelled with a detection probe) and the capture line. Understanding this, we theorised that we could predict the

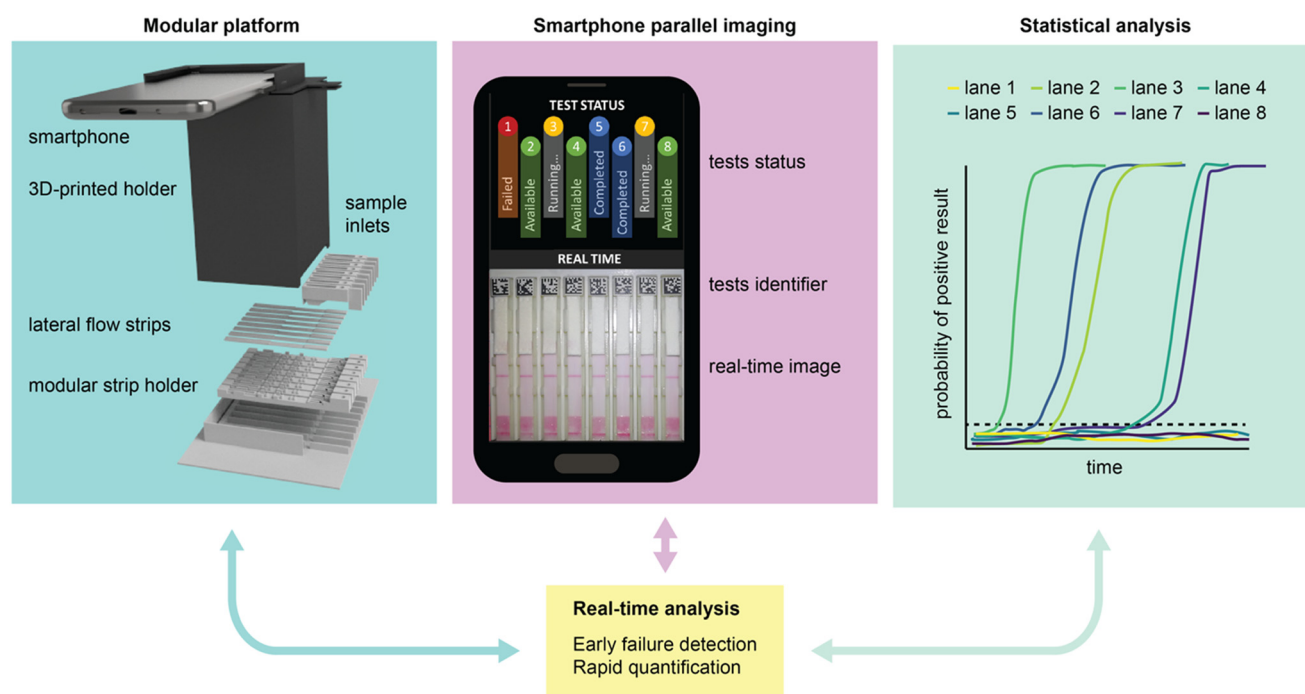


**Fig. 1** Overview of the LFIA processing platform, combining a 3D-printed modular platform, smartphone-assisted imaging, and advanced statistical analysis to monitor and read LFIA tests in real time.



end point of a test (*i.e.* positive or negative) by monitoring early-stage colour changes at the test line. In doing so, we hoped to realise significant time savings over traditional end-point readouts. To this end, we developed a thresholding system in which we employ real-time imaging to determine the time point at which a signal at the test line becomes

statistically significant over the background (*i.e.* the threshold time). Briefly, continuous images of the test strip are taken as the assay runs, with each frame being fed into a custom code. The code automatically crops the images and converts them to greyscale before identifying the regions of interest (ROIs; test line, control line, background) (Fig. 2).

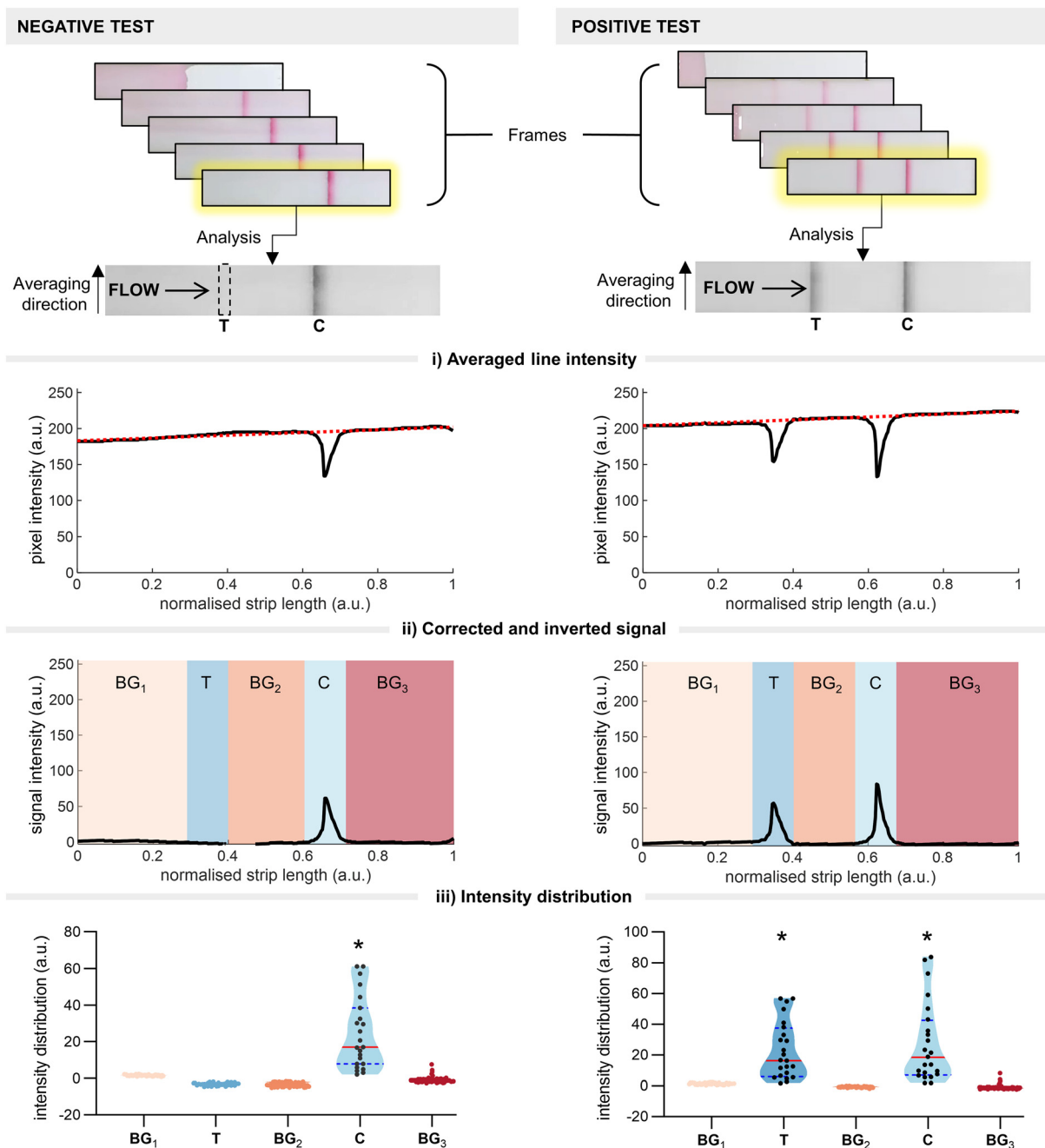


**Fig. 2** Example of an intensity analysis performed by the algorithm for detecting the control (C) and test (T) lines. i) For each frame, the pixel intensity (0–255 a.u.) is averaged along the vertical direction, as shown on the top portion of the figure for both *negative* and *positive* test examples. Due to inconsistent light conditions (caused by distance from the light source) the strip intensities increase linearly (as shown by the dotted red line). This information is used to correct the signal. ii) The signal is then inverted, obtaining a positive signal intensity (a.u.) for the control and test line regions. iii) The intensity distributions for each sub-region (test line, control line, BG<sub>1</sub>, BG<sub>2</sub>, and BG<sub>3</sub>) are calculated. The test is considered positive if the test line distribution is significantly higher than the background regions. A similar analysis is performed on the control line to ensure the validity of the test. \*: probability  $\alpha < 0.05$ .





The code then calculates the average intensity within the ROIs and applies a baseline correction (Fig. 2i). The test line is considered present if the intensity distribution is significantly higher than the background regions (Fig. 2ii and iii). Once the presence of a test line is confirmed, the intensity distribution is then analysed for statistical significance; the signal is considered significant if the following conditions are met:

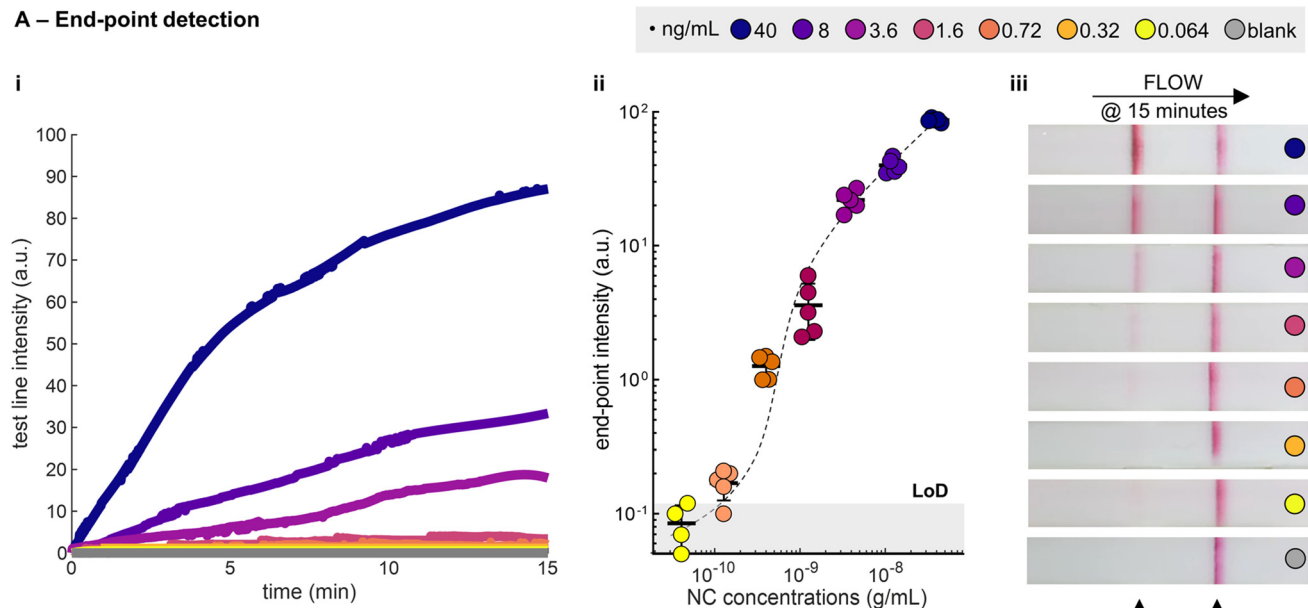
1) The current intensity spatial distribution at the test line differs significantly (probability  $\alpha < 0.05$ ) from the prior intensity spatial distribution for at least 1 second;

2) The current intensity spatial distribution at the test line differs significantly ( $\alpha < 0.05$ ) from the signal acquired in the first ten seconds after the flow front passes the test region.

Once these requirements are satisfied, the test is deemed positive. If the above criteria are not met once the maximum assay time (as defined by the manufacturer) is reached, the test is deemed negative. The computational process is described in detail in the Methods section.

To demonstrate the potential of real-time thresholding, we compared our statistical thresholding method to traditional end-point readout (Fig. 3A and B). We ran a dilution series of

### A – End-point detection



### B – Real-time thresholding

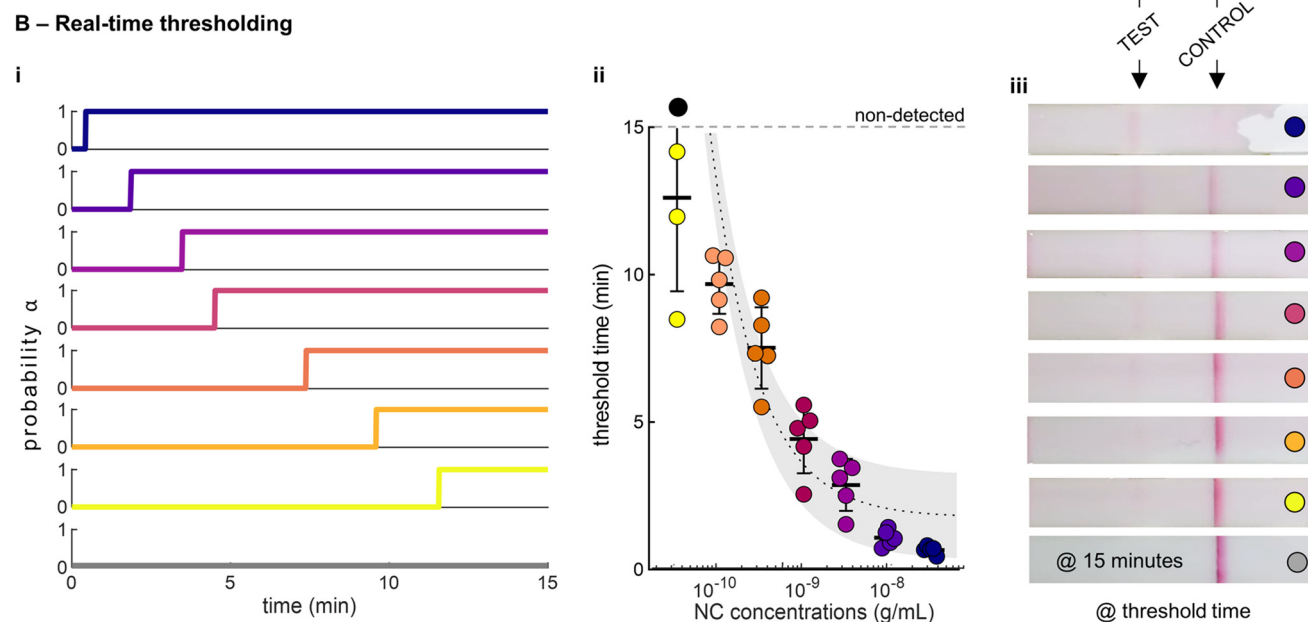


**Fig. 3** Results of line quantification, following (A) standard end-point readout or (B) statistical thresholding: (i) decision variable (test line intensity for end-point readout and probability  $\alpha$  for real-time detection) as a function of time; (ii) variation of the end-point intensity (top) and threshold time (bottom) as a function of nucleocapsid (NC) concentration. The LoD (top) is shown in grey and non-detected samples (bottom) are shown in black above the dotted line; (iii) images of the test strips at the time of reading.



SARS-CoV-2 nucleocapsid (NC), spiked into extraction buffer, on a commercial LFIA until completion (15 minutes, as defined by the manufacturer), and recorded the tests using a smartphone. We subsequently analysed the videos using a custom MATLAB script, as defined in the Methods section. The trends of the test line intensity from the recorded videos reflect the standard pseudo-first order binding kinetics (Fig. 3Ai), and the end-point test line intensities follow a Langmuir adsorption model (Fig. 3Aii, S3†). Using the intensity values at 15 minutes, we computed the limit-of-detection (LoD) as  $0.12 \text{ ng mL}^{-1}$  (defined from the blank mean intensity + 3 standard deviations). As anticipated, statistical detection results in threshold times that vary with NC concentration, with the highest concentrations giving statistically detectable signals at the shortest threshold times (Fig. 3Bi). The threshold times decrease with increasing NC concentrations and can be approximated using an inverse relationship (Fig. 3Bii and S4†). Visual inspection of the test strips at both the end-points and the threshold times demonstrates the differences between the two approaches (Fig. 3Aiii and Biii).

It is worth mentioning that the same definition of LoD (blank mean + 3 standard deviations) cannot be applied to the real-time thresholding approach, as blank tests do not have a defined threshold time (infinite time). Instead, the strictest definition of LoD is used, *i.e.* the lowest concentration that can be consistently detected (>97.5%). In this case, we report a LoD of  $0.32 \text{ ng mL}^{-1}$  (100% detected,  $n = 5$ ). Below this concentration we observed undetected samples (75% detected,  $n = 4$ ). Unsurprisingly, end-point and real-time approaches have similar LoDs. However, it is clear that the real-time thresholding method leads to considerable time savings (>50%) at higher antigen concentrations (> $0.72 \text{ ng mL}^{-1}$ ).

Next, we decided to further explore the potential of real-time thresholding to significantly reduce assay times. To this end, we simulated a case study in which one hundred LFIA tests are performed. To enable a fair comparison, we consider that only a single test is running at a given time (see section 2.3 for parallel processing). The positive test rate (*i.e.* the number of tests returning a positive result, 40%) was obtained from the Swiss Federal Office of Public Health – FOPH (Fig. S5†), whereas NC concentrations were selected from patient titres in nasopharyngeal swabs recorded by Pollock *et al.*<sup>24</sup> Based on these data sets, we clustered individuals into positive detectable and negative/positive non-detectable cohorts and computed the associated threshold time by interpolation from the curve obtained from non-linear regression of our previous dilution series (Fig. 4B). As previously described, we set the lower LoD for a positive result as  $0.32 \text{ ng mL}^{-1}$ .

Based on these data, we were able to demonstrate that for 100 tests performed under the simulated scenario (a 40% positive test rate, with titres between  $0.064\text{--}40 \text{ ng mL}^{-1}$ ), we could achieve time savings of  $\sim 17\%$  ( $17.1 \pm 2.6\%$ ) (Fig. 4C). Furthermore, by varying the positive test rate parameter we

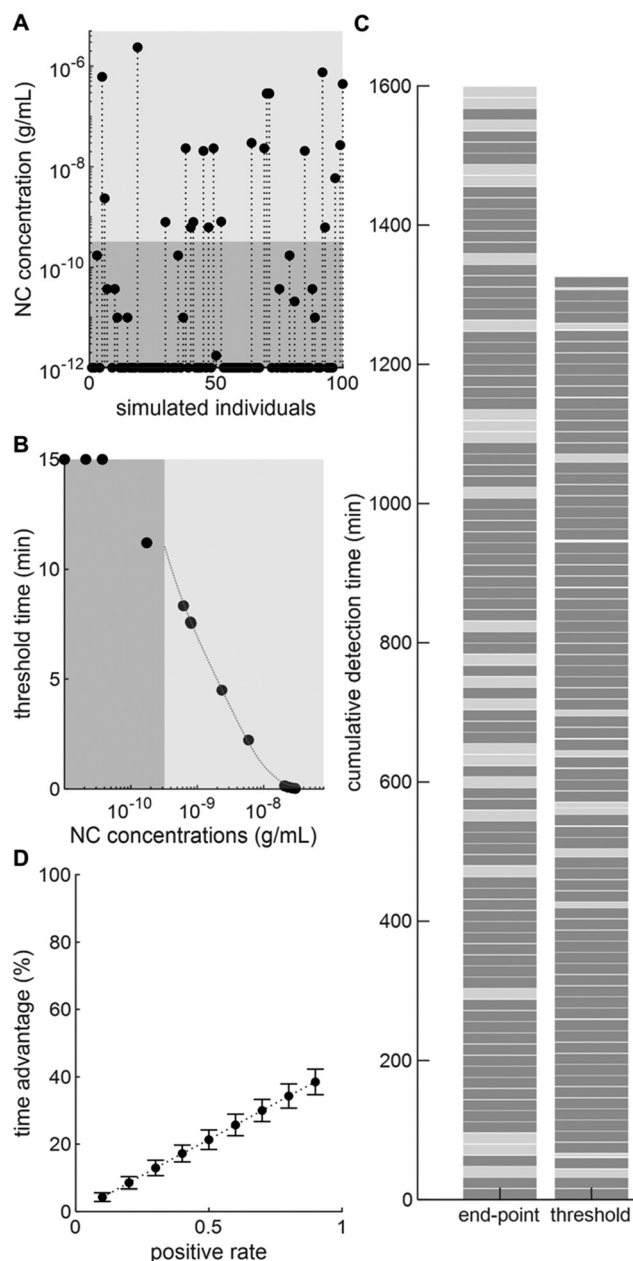


**Fig. 4** Analysis of time gain as a function of the positive rate, with the statistical line quantification method being compared to end-point detection. (A) Stem plot of the randomly attributed nucleocapsid concentration values. The samples are separated into a negative population (dark grey band) consisting of true negatives and non-detectable positives (*i.e.* below the limit of detection), and a positive population (light grey band). (B) The corresponding threshold time obtained for each random positive nucleocapsid concentration, based on interpolation of the dilution series in Fig. 3Bii. (C) The time advantage gained by employing statistical thresholding compared to a standard end-point readout shown for a positive rate of 40%. The simulation is based on 100 analyses performed in series. (D) Time gain compared to end-point readout as a function of positive test rate.

observe a linear relationship between positive rate and time savings (Fig. 4D). This is expected, since in the extreme cases where all samples are negative, the test needs to run for the full 15 minutes before a negative result can be called.



Accordingly, in such a scenario the thresholding method would provide no time saving. At the other extreme, where all samples are positive, we achieve much larger time gains (up to 40%). In summary, real-time thresholding has the potential to outperform end-point analysis in real-world scenarios and could provide significant time savings during infectious disease outbreaks.

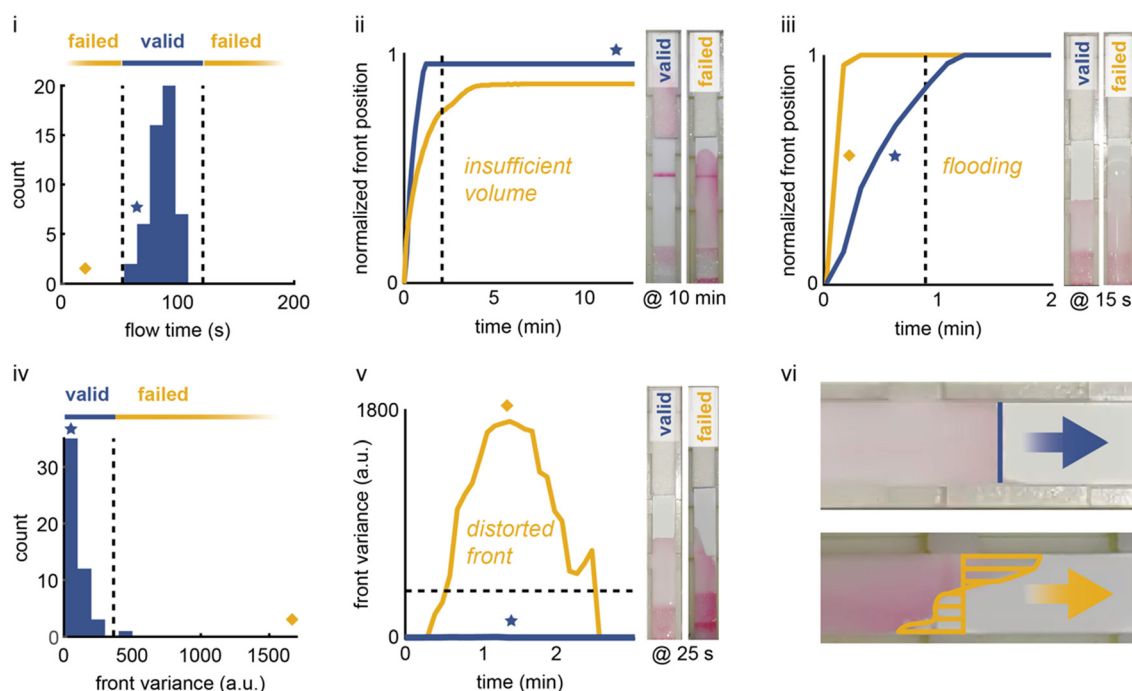
## 2.2 Early failure detection

The ongoing COVID-19 pandemic has triggered a surge in the development and deployment of LFIA tests, with more than 1019 individual tests for SARS-CoV-2 antigen and/or antibody detection certified with the European CE-IVD Marking (as of

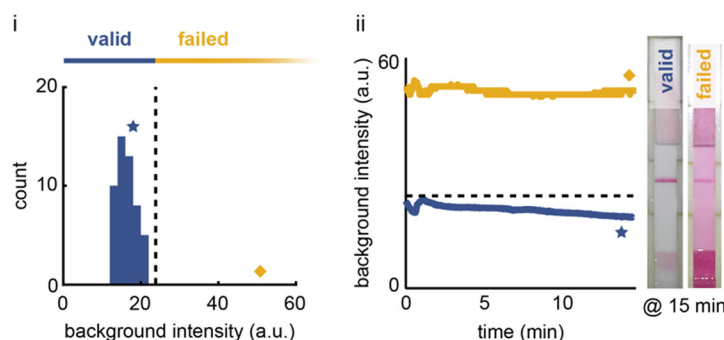
October 2022).<sup>25</sup> During the evaluation of these commercial LFIA tests, most publications have reported a low percentage (<2.5%) of invalid tests.<sup>26–30</sup> However, for many LFIA tests, the rate of failed/inconclusive results can be as high as 30%.<sup>26</sup> Evaluating failure rates is important, as failures lead to invalid or inconclusive results or false negatives/positives. This in turn leads to unnecessary treatments or otherwise irrelevant interventions that are likely to carry serious health, social and economic consequences.<sup>31,32</sup>

During our study, we observed that many causes of test failure manifest as irregularities in the flow profiles of the antigen–nanoparticle immunocomplexes, differences in intensities at the test and control lines, and increased background signals. Furthermore, we realised that many of

### A - Disturbed flow



### B - High background



### C - No control line

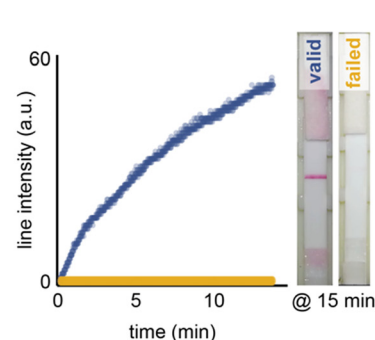


**Fig. 5** Early detection of LFIA failures through real-time image processing. The flow front (A) is monitored during the initial wetting phase. The time to reach the absorbent pad is determined and compared to a fully functional test (i). Abnormally slow (ii) or fast (iii) flow fronts are flagged by the algorithm. The shape of the front (iv) is also assessed, since a distorted front is indicative of device defects (v and vii). The colour intensity of the background (B) and the control line (C) are also checked at the end of the run to ensure that the values are within the expected range. Additional descriptions and illustrations of these failure scenarios can be found in Fig. S9.†



these manifestations could be detected using real-time imaging. Before investigating this, it was first necessary to identify possible causes of failures and link them to observables detectable using real-time imaging. Considering the entire life cycle of an LFIA test, we identified failures arising from issues related to manufacturing, storage or user operation (for details see the ESI†). Across these three categories, we have identified five classes of observables caused by LFIA failures: (i) disturbed flow profile, (ii) high relative background signal, (iii) lack of a control line, (iv) false negative (no test line with target present) and (v) false positive (test line visible in the absence of target) (Fig. S6†). Of these, the first three can be detected through real-time imaging, while the last two will go undetected. It is important to note that these observables are not independent, and we can expect a 'cascade effect' if one of them is present. For example, a sample flood will lead to a false negative, due to the decreased residence time of the immunocomplex at the test/control line. Based on the three identified detectable observables, we designed algorithms to automatically flag events indicative of test failure.

**Disturbed flow profile.** To detect test failures that manifest as disturbed flow profiles, the algorithm continuously monitors the flow profile (front speed and shape) of the test as it runs (Fig. S7†). This allows detection of common test failures such as clogging or insufficient sample volume, sample overloading (flooding), and manufacturing defects resulting in poor contact between the sample pad and test strip. To detect clogging or insufficient sample volume, we set a maximum time for the flow front to reach the absorbent pad. The wetting of commercial nitrocellulose membranes is reported as the capillary flow time by manufacturers (units: s/4 cm). For this particular test, under normal operating conditions, the flow front should reach the pad within  $90 \pm 10$  seconds (Fig. 5Ai). A significant increase in the time to reach the absorbent pad indicates insufficient sample volume (Fig. 5Aii); in our case, we set the maximum threshold at 122 seconds ( $\alpha < 0.05$ ). Similarly, a significant decrease in the time for the flow front to reach the absorbent pad indicates sample flooding (Fig. 5Aiii). This can be caused by overly large sample volumes, defective test strip cassettes, or device manipulation during operation. A decrease in residence time on the strip will negatively impact binding kinetics and thus the test result. Based on the expected flow rates under normal operating conditions, we set the minimum residence time as 53 seconds (probability  $\alpha < 0.05$ ). To detect distorted flow fronts, which are indicative of poorly assembled LFIA tests and poor pad contacts, we designed the algorithm to monitor the shape of the flow front (Fig. S8†). A failure is flagged if the variance of the front position along the dimension perpendicular to the flow overcomes a predetermined threshold based on the values obtained from a functional test (Fig. 5Aiv).

**High relative background signal.** To detect test failures due to high non-specific binding, typically caused by membrane or nanoparticle degradation, we designed the

algorithm to monitor the background colour intensity of the strip, excluding the test and control lines. Test failure is flagged if the intensity of the background rises above a predetermined threshold based on the values obtained from functional tests (Fig. 5B).

**No control line.** To detect test failures resulting from nanoparticle or control line defects, or improper storage, we designed the algorithm to monitor the presence of the control line on the strip. In this case, we used a binary YES/NO system with regard to the presence of the control line. A NO value indicated a test failure. (Fig. 5C).

It is important to note that all thresholds determined herein are defined for a specific LFIA device, type of sample specimen, and operational procedure. In our study, the use of an extraction buffer for nasopharyngeal swabs samples is advantageous as it provides for controlled sample properties and ensures consistent operation. It is expected that the detection of analytes in complex matrices, such as undiluted saliva or whole blood, will lead to broader variations of flow profiles and background intensities. In these assays, failures are more likely and their early detection by an automated imaging system would be highly valuable.

### 2.3 Smartphone-based real-time parallel platform

After verifying the potential benefits of early failure detection and real-time thresholding, we decided to integrate these methods directly into a smartphone App. Combined with a custom housing (Fig. S1 and S2†), this allows end-users to analyse multiple tests in parallel, all in real-time. We also coded additional features into the App, such as user registration and results display. The workflow of the App is briefly described in Fig. 6A. After registration of the user and insertion of the tests into the housing, the App pulls a frame from the video stream to perform an initial pre-processing step. The App checks for the presence of strips in each of the eight lanes using the unique QR codes located at the top of each insert. These QR codes are also used to link the tests to the unique identifiers assigned during registration. The App then uses the location of the QR codes and automated object recognition of the strip edges to delimit each individual test and create distinct regions of interest (ROIs) (Fig. S10†). The ROIs are then colour-converted into grayscale values and the background subtracted through linear approximation. The isolated, grayscale, and background subtracted test strips then enter the real-time detection phase, which combines the previously described failure analysis and statistical thresholding. For early failure detection, each strip is analysed frame-by-frame and features such as the shape and position of the liquid front and background intensity are used to determine test validity. Once the test is deemed valid, the pixel intensity at both the test line and control line is quantified for each frame. After satisfying the threshold conditions (as defined in section 2.1), a final check for signal intensity at the control line is made to rule out an invalid test. The results for that particular test are then displayed on





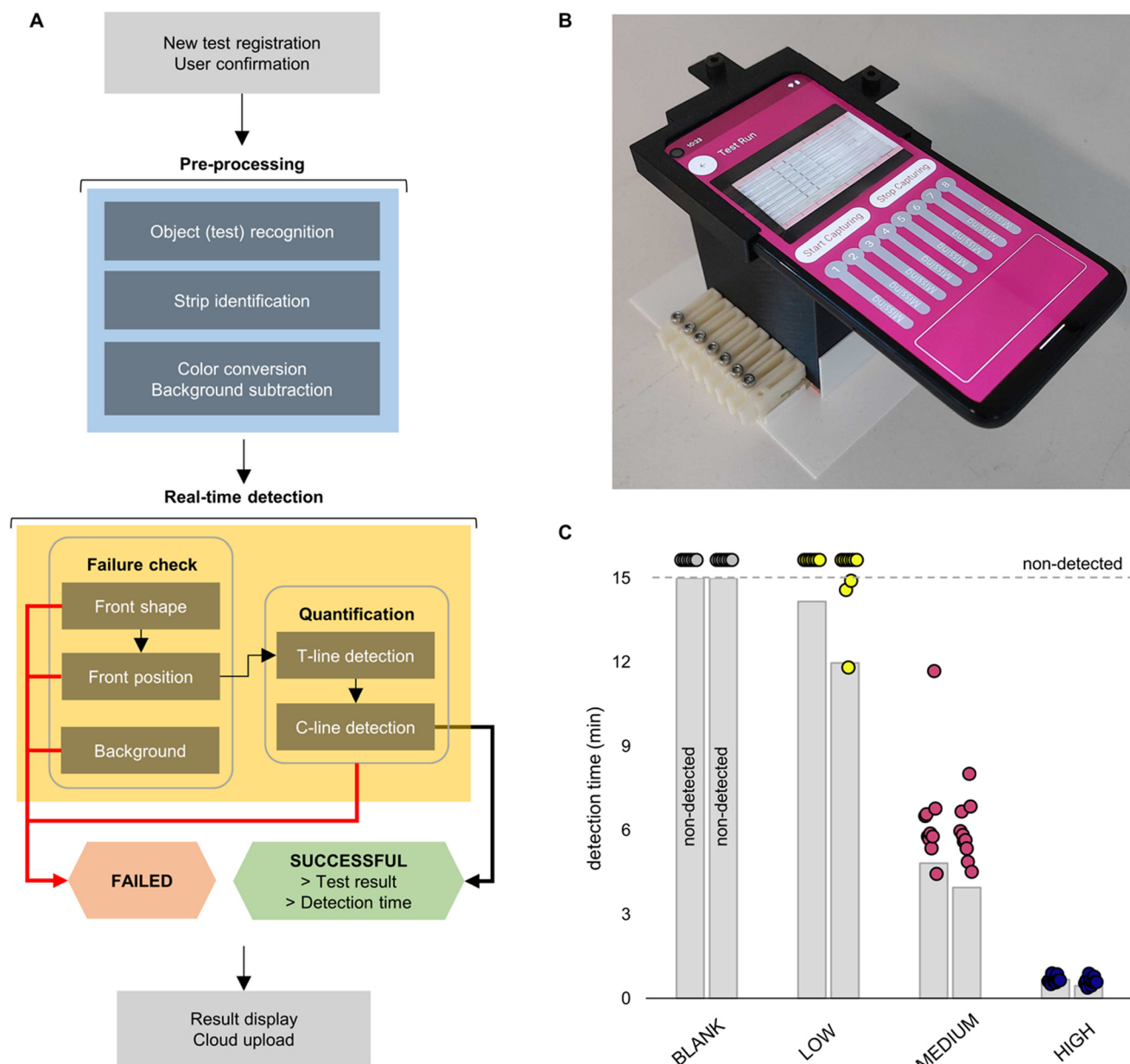


**Fig. 6** (A) A flowchart of the implemented smartphone App for real-time detection; (B) an image of the modular set-up, including the 3D-printed structure and the smartphone; (C) time-to-result through the App and by the naked eye detection for low ( $0.064 \text{ ng mL}^{-1}$ ), medium ( $1.6 \text{ ng mL}^{-1}$ ), and high ( $40 \text{ ng mL}^{-1}$ ) NC concentrations. Each concentration was run in duplicate and analysed by ten participants. The grey bars represent the real thresholding time for the specific test used in this analysis. The dots indicate the detection times (test line) for the eight tests at various NC titres. When the individual did not detect the T-line (for both the blank and low-concentration tests), the dots are located above the dashed line.

the App (Fig. 6A and B). The entire process is random access; complete tests can be removed and replaced by a new test whilst other tests are running, and the process begins again. This prevents low-titre samples or negatives from causing a bottle-neck in the testing process and ensures maximal throughput. The entire testing process is further detailed in Fig. S11.†

In addition to comparison with standard end-point signal readout, the App's functionality was evaluated against human readout. In brief, eight LFIA tests were divided into four categories: blank tests, and low ( $0.064 \text{ ng mL}^{-1}$ ), medium ( $1.6$

$\text{ng mL}^{-1}$ ), and high ( $40 \text{ ng mL}^{-1}$ ) NC concentrations. The lanes were randomly placed in the set-up and a full video of the test run was recorded. Along with the detection time measured through the App, ten human volunteers were asked to monitor the video and record the earliest time at which they could see the test line. While no difference in performance was observed for the highest concentration and blank tests, the time advantage at medium was notable (average time gain 2.2 minutes per test) (Fig. 6C). Moreover, out of the ten volunteers, the test line for low concentrations was successfully detected only in 20% of cases; the remaining

tests (80%) were assigned as negative. This contrasts with the App, which assigned every test correctly. Accordingly, our detection system proved to be more effective, especially at lower antigen concentrations.

### 3. Conclusions

To conclude, we have presented a robust method for improving the throughput of LFIA testing by leveraging the power of parallelised real-time image analysis. This method leverages automated computational image processing to continuously monitor test line intensity, background, control line presence, and sample flow profiles. By exploiting the wealth of information gleaned from this continuous analysis, our approach significantly decreases the time-to-result and facilitates the early detection of test failures. Finally, we integrated our code into a smartphone App capable of automatically analysing up to eight tests in parallel and demonstrated significant improvements in testing performance compared to conventional human readout. This work highlights the potential of real-time imaging to augment and enhance lateral flow testing workflows and significantly improve testing throughput in point-of-need scenarios. Moving forwards, we anticipate that real-time automated imaging could be used to similarly improve the testing throughput of various colourimetric/fluorimetric biosensing diagnostic assays and become an established tool within point-of-need testing.

## Methods

### 3D-printed platform

The smartphone holder and main enclosure were printed using a fused deposition modelling (FDM) 3D printer (MK3S, Prusa Research) with a polyethylene terephthalate glycol (PETG) filament (Prusament PETG, Prusa Research) and standard printing parameters. The strip holders and inlets were printed using a stereolithography (SLA) 3D printer (SL1, Prusa Research) and ABS-like resin (PrimaCreator Tough, Prusa Research) with the recommended printing parameters. Once the strip was inserted in the strip holder, the inlet was screwed on with an M3 screw. All parts were designed in FreeCAD and the STL 3D model can be found in the Supplementary Materials.

### Lateral flow tests

A SARS-CoV-2 Rapid Antigen Test (Roche Diagnostics) was used as a model LFIA system. The strips were removed from the cassette and inserted in our in-house developed holders to fit in the imaging platform. The nasopharyngeal extracting buffer provided with the rapid tests was spiked with SARS-CoV-2 nucleocapsid recombinant (LA612, EastCoast Bio). A volume of 100  $\mu\text{L}$  was injected into the LFIA inlet and the strips were imaged for up to 15 minutes. Failures were simulated by damaging critical points of the LFIA tests or by altering the concentration of gold nanoparticles.

### Computational methods

Videos (60 fps) of the LFIAs were analysed frame-by-frame, and in-house developed algorithms were used to segment and identify the ROIs. The algorithms, written in MATLAB (R2022a, Natick, MA, USA), were then converted into C++ (ISO C11+) through MATLAB Coder. The C++ code was generated for a generic device with 64-bit Embedded Processor.

### Smartphone App

The smartphone App was designed using the Flutter framework developed by Google (License BSD 3-Clause). This framework allows for App deployment to iOS and Android phones with a single App source code. The algorithms used for the image analysis of the LFIAs, once developed in MATLAB and converted into C++ scripts, are introduced as an in-house developed plugin. The source code of the smartphone App was written with the aid of integrated developments environments Android Studio (Google and JetBrains) and CLion (JetBrain). An Android phone (Huawei, P10 Plus, 2017) was employed to acquire the recordings and run the smartphone App.

### Statistical analysis

Statistical line detection is based on the differences among the intensity distributions of the test strip. In particular, a Mann Whitney *U*-test was employed to detect significantly different intensity values for the test- and control-line regions compared to background regions. Mean and standard deviation or median and interquartile range were used where appropriate (following the Kolmogorov-Smirnov normality test). Five repetitions were considered for each NC titre, and median values were extracted.

### Human readout

To compare our computational method and human naked-eye readout, we recruited ten volunteers ( $27.2 \pm 3.6$  years old) to participate in a controlled study. The device and smartphone were set up to run eight tests in parallel, in a randomised order from left to right, and the results were stored anonymously. The feed from the smartphone was recorded for later playback to the human participants. Each participant was then placed individually and separately in front of a monitor and instructed to record the first time instant when they could detect the test line for each test. The lighting conditions and distance from the monitor were consistent for each test. Five individuals (50%) wore corrective glasses/contact lenses, and no statistical difference in the performance of the two groups was found. Participants were screened for colour blindness and no cases were reported.

## Acronyms & Abbreviations

NC	Nucleocapsid
C	Control



T Test

LFIA Lateral flow immunoassay

ROI Region of interest

LoD Limit-of-detection

## Author contributions

M. C. designed and coded the computational image analysis algorithms, performed the comparison with human subjects, and performed statistical analysis; L. B. designed and manufactured the custom housing and inserts, ran the LFIAs, and determined the causes of LFIA failure; A. R. T. designed and coded the App; D. A. R. conceived and managed the project; M. C., L. B., and D. A. R. wrote the first draft of the manuscript; C. J. S. provided supervision and resources. A. J. D. M. provided supervision, resources, and edited the final draft of the manuscript.

## Conflicts of interest

There are no conflicts to declare.

## Acknowledgements

D. A. R. acknowledges funding from the European Union's Horizon 2020 research and innovation programme under the Marie Skłodowska-Curie grant agreement 840232. M. C. acknowledges funding from Fondation Botnar (Basel, Switzerland), through the project titled "Development and Validation of a Lateral Flow Test to Detect COVID-19 Immunity in Saliva (DAVINCI)".

## References

- 1 D. E. Charlton, Church and Dwight Co Inc, United States, US6485982B1, 2002.
- 2 E. B. Bahadır and M. K. Sezgentürk, *TrAC, Trends Anal. Chem.*, 2016, **82**, 286–306.
- 3 S. Rosen, in *Lateral Flow Immunoassay*, ed. R. Wong and H. Tse, Humana Press, Totowa, NJ, 2009, pp. 1–15.
- 4 H. R. Boehringer and B. J. O'Farrell, *Clin. Chem.*, 2022, **68**, 52–58.
- 5 Y. Zhang, Y. Chai, Z. Hu, Z. Xu, M. Li, X. Chen, C. Yang and J. Liu, *Front. bioeng. biotechnol.*, 2022, **10**, DOI: [10.3389/fbioe.2022.866368](https://doi.org/10.3389/fbioe.2022.866368).
- 6 A. Suea-Ngam, L. Bezing, B. Mateescu, P. D. Howes, A. J. de Mello and D. A. Richards, *ACS Sens.*, 2020, **5**, 2701–2723.
- 7 A scoping review of point-of-care testing devices for infectious disease surveillance, prevention and control, <https://www.ecdc.europa.eu/en/publications-data/scoping-review-point-care-testing-devices-infectious-disease-surveillance>, (accessed 12 October 2022).
- 8 K. Lukaszuk, J. Kiewisz, K. Rozanska, M. Dabrowska, A. Podolak, G. Jakiel, I. Woclawek-Potocka, A. Lukaszuk and L. Rabalski, *Vaccines*, 2021, **9**, 840.
- 9 N. K. Khosla, J. M. Lesinski, M. Colombo, L. Bezing, A. J. deMello and D. A. Richards, *Lab Chip*, 2022, **22**, 3340–3360.
- 10 J. J. Deeks, A. Singanayagam, H. Houston, A. J. Sitch, S. Hakki, J. Dunning and A. Lavani, *BMJ*, 2022, **376**, e066871.
- 11 D. S. Mouliou and K. I. Gourgoulanis, *Expert Rev. Respir. Med.*, 2021, **15**, 993–1002.
- 12 ECDC Technical Report, Considerations on the use of self-tests for COVID-19 in the EU/EEA, 17th March 2021.
- 13 C. S. Wood, M. R. Thomas, J. Budd, T. P. Mashamba-Thompson, K. Herbst, D. Pillay, R. W. Peeling, A. M. Johnson, R. A. McKendry and M. M. Stevens, *Nature*, 2019, **566**, 467–474.
- 14 L. P. Bheemavarapu, M. I. Shah, J. Joseph and M. Sivaprakasam, *Biosensors*, 2021, **11**, 211.
- 15 A. E. Urusov, A. V. Zherdev and B. B. Dzantiev, *Biosensors*, 2019, **9**, 89.
- 16 Lateral Flow Reader| From home to lab use, <https://www.lateralflowreader.com/>, (accessed 12 October 2022).
- 17 operon, OPERON Lateral Flow Reader, <https://operondx.com/operon-lateral-flow-reader/>, (accessed 12 October 2022).
- 18 V. Turbé, C. Herbst, T. Mngomezulu, S. Meshkinfamfard, N. Dlamini, T. Mhlango, T. Smit, V. Cherepanova, K. Shimada, J. Budd, N. Arsenov, S. Gray, D. Pillay, K. Herbst, M. Shahmanesh and R. A. McKendry, *Nat. Med.*, 2021, **27**, 1165–1170.
- 19 Y. Jung, Y. Heo, J. J. Lee, A. Deering and E. Bae, *J. Microbiol. Methods*, 2020, **168**, 105800.
- 20 V. Turbé, E. R. Gray, V. E. Lawson, E. Nastouli, J. C. Brookes, R. A. Weiss, D. Pillay, V. C. Emery, C. T. Verris, H. Yatsuda, D. Athey and R. A. McKendry, *Sci. Rep.*, 2017, **7**, 11971.
- 21 N. C. K. Wong, S. Meshkinfamfard, V. Turbé, M. Whitaker, M. Moshe, A. Bardanzellu, T. Dai, E. Pignatelli, W. Barclay, A. Darzi, P. Elliott, H. Ward, R. J. Tanaka, G. S. Cooke, R. A. McKendry, C. J. Atchison and A. A. Bharath, *Community Med.*, 2022, **2**, 1–10.
- 22 Lateral Flow Fluorescence Measurement|ESEQuant LR3, <https://www.lateralflowreader.com/esequant-lr3/>, (accessed 12 October 2022).
- 23 B. S. Miller, C. Parolo, V. Turbé, C. E. Keane, E. R. Gray and R. A. McKendry, *Chem. – Eur. J.*, 2018, **24**, 9783–9787.
- 24 N. R. Pollock, T. J. Savage, H. Wardell, R. A. Lee, A. Mathew, M. Stengelin and G. B. Sigal, *J. Clin. Microbiol.*, 2021, **59**, e03077-20.
- 25 Home| COVID-19 In Vitro Diagnostic Devices and Test Methods Database, <https://covid-19-diagnostics.jrc.ec.europa.eu/>, (accessed 12 October 2022).
- 26 M. C. Tollånes, A.-M. B. Kran, E. Abildsnes, P. A. Jennum, A. C. Breivik and S. Sandberg, *Clin. Chem. Lab. Med.*, 2020, **58**, 1595–1600.
- 27 J. Dinnes, J. J. Deeks, A. Adriano, S. Berhane, C. Davenport, S. Dittich, D. Emperador, Y. Takwoingi, J. Cunningham, S. Beese, J. Dretzke, L. F. di Ruffano, I. M. Harris, M. J. Price, S. Taylor-Phillips, L. Hooft, M. M. Leeflang, R. Spijker, A. V. den Bruel and C. C.-19 D. T. A. Group, *The Cochrane Database of Systematic Reviews*, 2020.
- 28 G. C. Mak, P. K. Cheng, S. S. Lau, K. K. Wong, C. Lau, E. T. Lam, R. C. Chan and D. N. Tsang, *J. Clin. Virol.*, 2020, **129**, 104500.



- 29 N. Kohmer, S. Westhaus, C. Rühl, S. Ciesek and H. F. Rabenau, *J. Clin. Virol.*, 2020, **129**, 104480.
- 30 V. M. Corman, V. C. Haage, T. Bleicker, M. L. Schmidt, B. Mühlemann, M. Zuchowski, W. K. Jo, P. Tscheak, E. Möncke-Buchner, M. A. Müller, A. Krumbholz, J. F. Drexler and C. Drosten, *Lancet Microbe*, 2021, **2**, e311–e319.
- 31 S. N. Ladhani, J. Y. Chow, S. Atkin, K. E. Brown, M. E. Ramsay, P. Randell, F. Sanderson, C. Junghans, K. Sendall, R. Downes, D. Sharp, N. Graham, D. Wingfield, R. Howard, R. McLaren and N. Lang, *J. Infect.*, 2021, **82**, 282–327.
- 32 Y. Shimazu, Y. Kobashi, T. Zhao, Y. Nishikawa, T. Sawano, A. Ozaki, D. Obara and M. Tsubokura, *Clin. Case Rep.*, 2021, **9**, e04122.

